mater.scichina.com link.springer.com

Published online 4 November 2022 | https://doi.org/10.1007/s40843-022-2222-6
Sci China Mater 2023, 66(3): 1079–1088

Theoretical studies of non-noble metal single-atom catalyst Ni_1/MoS_2: Electronic structure and electrocatalytic CO_2 reduction

Qi Yu*

ABSTRACT **Single-atom catalysts (SACs) have aroused significant interest in heterogeneous catalysis in recent years because of their high catalytic selectivity and tunable activity in various chemical reactions. Herein, non-noble metal SACs with 3d-series metal single atoms (M_1) (M = Sc, Ti, V, Cr, Mn, Fe, Co, Ni, Cu, Zn) supported on MoS_2 are computationally screened by using first-principles quantum-chemical theory. The Ni_1/MoS_2 catalyst is found to be the most stable among those 3d-series SACs due to the optimal binding energy. In order to provide a fundamental understanding of the intrinsic stability and bonding interaction between the metal single atoms and MoS_2 support, the electronic structure, including the spin density populations, charge density difference (CDD), electron localization function (ELF), band structure, density of states (DOS), and crystal orbital Hamiltonian populations (COHP) are systematically examined. The solid-state quantum theory of atoms in molecules (QTAIM) is also applied to further characterize the Ni–S and Mo–S covalent and ionic bonding nature between the metal single atoms and support. It is found that in addition to Ni–S bonding, there exists significant Ni–Mo bonding that is critical for the electronic structure, stability, and catalytic properties of Ni_1/MoS_2 catalyst. As a typical application of this Ni_1/MoS_2 catalyst, the electrocatalytic mechanism and reaction pathway of CO_2 reduction reaction (CO_2RR) on Ni_1/MoS_2 catalyst have been investigated. The MoS_2-supported Ni single atoms are found to exhibit high catalytic activity for CO_2RR to methanol. The calculational results provide theoretical insights towards the design of highly efficient SACs on MoS_2-based functional materials.**

Keywords: quantum theory of atoms in molecules, single-atom catalyst, electronic structure, electrocatalytic, CO_2 reduction

INTRODUCTION

Transition metal dichalcogenides have received extensive attention in recent years due to their distinct physical and chemical properties and robust performance in various applications [1–6]. Particularly, metal disulfides MS_2 (M = Cr, Mn, Fe, Co, Ni, Zn, Mo, W) have been widely studied for electrochemical applications [7–13]. Among these developed MS_2 materials, MoS_2 is identified as an ideal electrocatalytic candidate because of its highly manipulable doping geometries and characteristic electronic structures [14–18], which can be advantageous for CO_2 reduction [19,20]. Nevertheless, MoS_2 has limited electrocatalytic activity on account of its high-proportioned electrochemically inactive inter-area [21]. The restrictive electron transfer ability also puts restraint on the transport route of electrons, leading to low electrocatalytic reactivity [22]. There are two strategies to enhance the electrocatalytic efficiency of MoS_2: (1) increasing its intrinsic activity; (2) augmenting the number of active sites [23]. Currently, efforts have been made by introducing promoter cations, which can activate the inert S atoms of the basal plane [24].

Since Zhang, Li, Liu and colleagues [25] proposed the novel concept of single-atom catalyst (SAC) in 2011, the heterogeneous SACs have caused increasingly extensive interest in heterogeneous catalysis and bio-catalysis due to the highly efficient utilization of atoms and well-defined active centers [26–30]. Among them, the transition metal atoms have the advantage of controllable coordination geometries, electronic structures, and spin states of the active center, which can dictate the catalytic behavior and activity of SACs [28,31–33]. Different from nano-catalysts, the transition metal SAC's geometric, electronic, spin and magnetic states can be fine-tuned to generate desirable catalytic selectivity [34]. With these features, SACs can be delicately designed with MoS_2 support to ensure electronic conductivity and maximize the exposed active sites. Therefore, in-depth understanding of the enhancing effects of SACs needs to be established for promoting targeted catalytic reactions. With the emergence of new characterization techniques and synthesis strategies (e.g., defect engineering strategies, spatially constrained strategies, and coordinated design strategies [35]), SACs have been proven to be valuable in various catalytic reactions, including oxygen reduction reaction (ORR) [36–40], hydrogen evolution reaction (HER) [41], N_2 reduction reaction (NRR) [42–53], CO_2 reduction reaction (CO_2RR) [54–60], CO oxidation reaction (COOR) [61], and biomass conversion [27].

Electrochemical CO_2RR has been expected as a facile route for converting CO_2 to CO, alcohols, acids and other organics [62,63]. However, owing to the high stability of CO_2 molecules and the complicated reaction network, CO_2RR is kinetically slow and suffers from high overpotential, low Faradaic efficiency, and unsatisfactory selectivity. Moreover, the concurrent HER ($2H^+ + 2e^- \rightarrow H_2$) is vying on CO_2RR in aqueous electrolytes [64]. Therefore, it is interesting to explore MoS_2-based non-noble metal SACs for CO_2RR electrocatalysts for direct production of alcohols with high selectivity.

Herein, theoretical studies are carried out on the stabilities of SACs with the non-noble 3d-series of metal single atoms (M_1, M = Sc, Ti, V, Cr, Mn, Fe, Co, Ni, Cu, Zn) supported on MoS_2. It is

School of Materials Science and Engineering, Shaanxi Laboratory of Catalysis, Shaanxi University of Technology, Hanzhong 723001, China
* Corresponding author (email: qiyu@snut.edu.cn)

found that Ni_1/MoS_2 is the most stable SAC among those studied here, which is then selected as a typical example to explore the chemical bonding between the metal atoms and MoS_2 support surface. The electronic structures and electrocatalytic performance for CO_2RR with Ni_1/MoS_2 have been investigated in details.

THEORETICAL AND COMPUTATIONAL DETAILS

Theoretical calculations were carried out based on periodic density functional theory (DFT) using the Vienna *ab initio* simulation package (VASP 5.3.2) [65,66]. Generalized gradient approach (GGA) was applied using the Perdew-Burke-Ernzerhof (PBE) exchange-correlation functional [67]. The projector-augmented wave (PAW) method with scalar relativistic effects was adopted to account for the interaction of valence electrons and ionic core. The kinetic energy cutoff of 500 eV was used for the planewave basis set. The geometries were fully optimized by using the spin-polarized Kohn-Sham self-consistent field method with force convergence standard of 10^{-6} eV and 0.02 eV $Å^{-1}$, respectively. The Brillouin zone was sampled with a 3 × 3 × 1 Monkhorst-Pack *k*-point mesh for geometry optimizations and more accurate 5 × 5 × 1 mesh was used for MoS_2 electronic structure analysis. The Bader charges were also calculated to investigate the charge population [68]. Meanwhile, the charge density difference between the fragments (A, B) and the combined A+B was calculated by $\Delta\rho = \rho_{A+B} - \rho_A - \rho_B$, where ρ represents the total electron density.

The 3 × 3 × 1 MoS_2 monolayer supercell (containing 27 atoms) with a 15-Å vacuum region was used to avoid the artificial interaction among adjacent image units. The binding energy (ΔE_{M_1}) of the metal single atom supported on MoS_2 was calculated as

$$\Delta E_{M_1} = E_{M_1/MoS_2} - E_{M_1} - E_{MoS_2},$$

where E_{M_1/MoS_2}, E_{M_1}, and E_{MoS_2} are the energies for the M_1/MoS_2, bulk metal unit cell-based single atom, and MoS_2 monolayer, respectively. As the energy of the metal single atom is referenced to the unit cell of bulk metal crystal ($E_{M_1} = E_{metal}/n$, here n is the number of metal atoms in the unit cell), all the binding energies of M_1 on MoS_2 are positive (i.e., endothermic), implying that the smaller the binding energy value is, the least endothermic the process is, and therefore the more stable the SAC becomes. The projected crystal orbital Hamilton population (COHP) was used to analyze the bonding properties between Ni and S atoms in the solid-state material [69].

In the electrochemical calculations, the Gibbs free energy of electrochemical CO_2RR was evaluated based on the computational hydrogen electrode (CHE) model proposed by Nørskov *et al.* [70]. Using the reversible hydrogen electrode (RHE), the free energy of $H^+ + e^-$ in aqueous solution was set to equal to 1/2 H_2, under standard conditions [71]. The free energy (ΔG) of a reaction at ambient temperature (T = 298.15 K) and pressure (P = 1 atm) was calculated as

$$\Delta G = \Delta E + \Delta E_{ZPE} - T\Delta S + e\Delta U,$$

where ΔE is the total reaction energy at the given temperature and pressure, ΔE_{ZPE} is the correction of zero-point energy, $T\Delta S$ is the entropy contribution, and $e\Delta U$ denotes the free energy change with the applied electrode potential.

Inasmuch as metal single atoms are bonded with MoS_2, ADF-Band program [72] was further utilized to investigate the single atom charges and metal-support bonding properties to determine the bond critical point (CP), bond path and other properties through a method based on Bader's quantum theory of atoms in molecules (QTAIM) [73]. These solid-state QTAIM calculations were performed with PBE functional and uncontracted TZ2P Slater basis functions which provide fundamental bonding data for SACs.

RESULTS AND DISCUSSION

Single atom binding and stability of M_1/MoS_2

For single atom binding on the MoS_2 monolayer, there are three high-symmetry inequivalent sites to be considered: (1) the top of Mo, (2) the top of S, and (3) the hollow site. For all 10 transition metals (from Sc to Zn) considered, two types of optimized stable structures are obtained: the hollow site (face-centered cubic: Sc, Ti, Mn) as shown in Fig. 1a, and the top of Mo (hexagonal close-packed: Fe, V, Cr, Co, Ni, Cu, Zn) (Fig. 1b), respectively. The bond length of M_1 to S atom ranges from 2.11 to 2.40 Å, implying significant M–S chemical bonding interaction. The exception is for Zn, which has a distance d_{M-S} of 3.52 Å, indicating chemically unbound Zn···S, consistent with the $d^{10}s^2$ closed shell of Zn. The S–M–S angles lie between 85.6° to 106.4° from Sc to Cu.

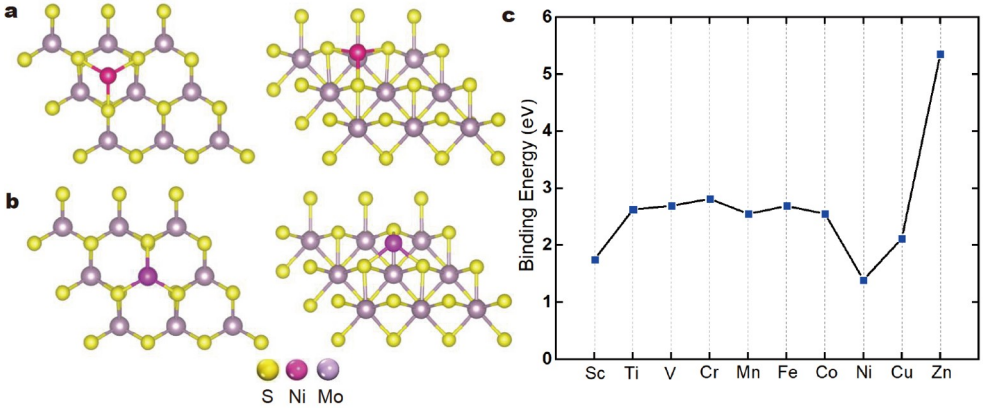

Figure 1 Optimized geometry structures and binding energy (ΔE_{M_1}) for M_1/MoS_2 (M = Sc–Zn) monolayers. Top view and 45° side-view for (a) the hollow site and (b) top site of Mo. (c) Binding energy ΔE_{M_1} for M_1/MoS_2 with metal single-atom energy obtained from the unit cell of bulk metal crystal.

The binding energy ΔE_{M_1} of M_1/MoS_2 is plotted in Fig. 1c. As mentioned earlier, all the binding processes of M_1 to MoS_2 are endothermic when the M_1 atom is taken from the bulk crystal. That is, the smaller positive binding energy represents higher stability of the SACs, which is in contrast to the exothermic (negative) binding energy calculated with reference to isolated M_1 atom. From Fig. 1c, while the least stable is Zn_1/MoS_2 with ΔE_{Zn} = 5.37 eV, the most stable is Ni_1/MoS_2 with ΔE_{Ni} = 1.39 eV, with Sc_1/MoS_2 and Cu_1/MoS_2 being the second and third most stable. The specific binding energy values calculated are listed in Table S1. These binding energies indicate that the M_1/MoS_2 SACs (except Zn) that have been considered in this study are possible targets for experimental synthesis. Given the theoretically predicted highest stability of Ni_1/MoS_2 among these SACs, the following section will focus on the electronic structures and electrocatalysis of this promising SAC hereafter.

To interpret the binding energy trend, the COHP was calculated to analyze the interaction between M_1 (M = Mn, Ni, Cu) and the nearest S atom (Fig. 2). The COHP information of other 3d-series transition metals M_1 (M = Sc, Ti, V, Cr, Fe, Co, Zn) to S is depicted in Fig. S1. In addition, the integrated COHP (ICOHP), which was obtained by integration of COHP over all levels up to the Fermi level, was also calculated. The ICOHP represents a particular bond's contribution to the band-structure energy, thus measuring the bonding strength (the more negative the ICOHP, the stronger the bonding strength). It turns out that there is a nearly linear correlation between ICOHP and ΔE_{M_1}, which gives a quantitative explanation for the M_1 binding strength to MoS_2 in terms of the bonding orbital populations. Therefore, the bonding orbital populations can be used to account for the observed trends for the binding energies of these metal single atoms. This finding is consistent with the novel covalent metal-support interaction (CMSI) previously found for SACs [74].

Spin and charge density difference of Ni_1/MoS_2

As the 3d-series of transition metals have radially rather contracted 3d orbitals, the spin properties of their SACs are essential for the catalytic properties. Fig. 3a (top and side panels) presents the spin densities of the MoS_2 monolayer. It reveals that, as expected, there is no obvious spin-polarization for MoS_2. In contrast, when the Ni single atom is supported on MoS_2, it has considerable spin polarization, as shown by the spin density analysis (Fig. 3b), which then causes slight spin polarization at the first nearest neighboring Mo atoms. Therefore, the Ni_1/MoS_2 material can be regarded as spin-polarized SAC through accommodating the magnetic structure of single atom-based sites [75,76].

To further investigate the origin of spin population and charge distribution of Ni_1/MoS_2, the following electronic structure analyses were carried out: (1) charge density differences obtained by comparing the total charge density from Ni_1 + MoS_2 and Ni_1/MoS_2, (2) Bader charges of Ni, Mo, and S atoms from the QTAIM analysis. Fig. 3c shows the charge density difference, from which one can see that the Ni atom has obviously transferred some electron density to the MoS_2 support. The transferred electron density from the Ni atom is primarily situated on the Ni–S bonding region. The two-dimensional (2D) charge density difference is shown in Fig. 3d, which again reveals that there is distinct charge transfer from the Ni atom area. The plane-averaged charge-density difference as calculated by using vaspkit is shown in Fig. 3e [77]. Along *Z*-coordination, the charge density difference changes from flat to major fluctuation near the Ni atom, and then becomes flat again. By means of the Bader charge analysis (Table S2), compared with the MoS_2 support, the Ni atom in Ni_1/MoS_2 has positive charge of $+0.39|e^-|$, which causes the electron density of Mo and S to increase by 0.16 and $0.02|e^-|$, respectively. That is, the electron density flows from Ni to Mo and S, which is consistent with the charge density difference results. The charge transfer between Ni and MoS_2 is responsible for the enhanced structure stability of SACs because of the ionic interaction between $Ni^{\delta+}$ and $S^{\delta-}$ [78,79], in addition to the CMSI.

DOS and band structure of Ni_1/MoS_2

To further investigate the electronic structure of the SACs under consideration, the total and projected electron density of states (DOS) and band structure of the MoS_2 support and Ni_1/MoS_2 were studied and the results are shown in Fig. 4a, c. For Ni_1/MoS_2, the change below −0.41 eV to Fermi level arises from the Ni–S bonding interaction as well as the d-states of Ni atoms.

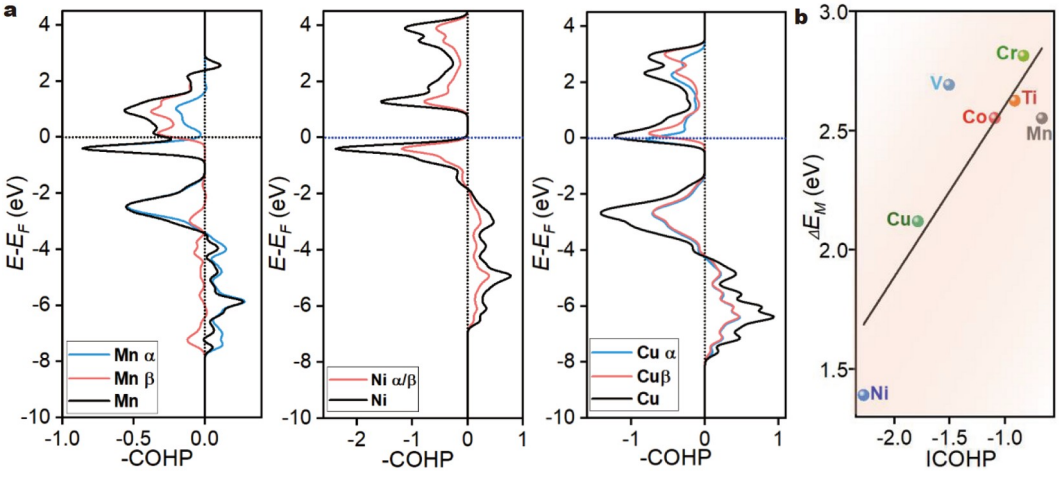

Figure 2 (a) The calculated –COHP between M_1 (M = Mn, Ni, Cu) and S atom of MoS_2. (b) Illustration of the linear correlation between the ICOHP and the binding energy of M_1/MoS_2 (ΔE_{M_1}).

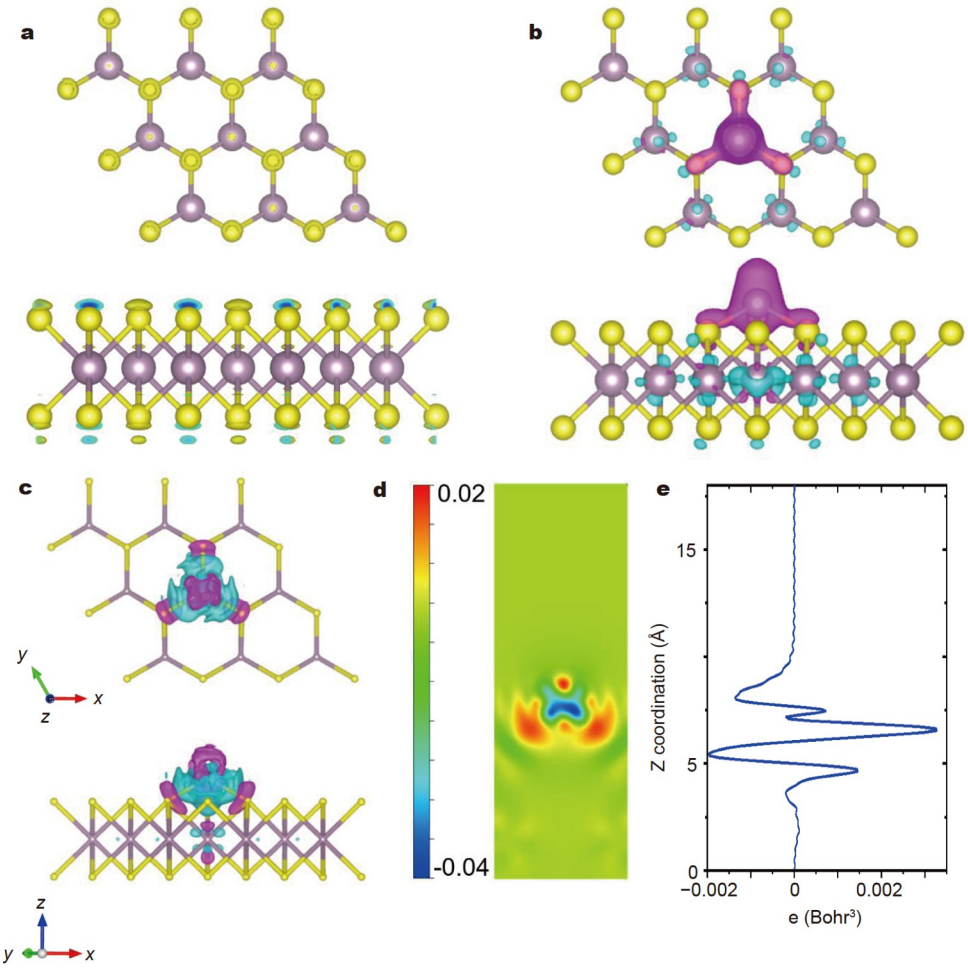

Figure 3 The spin densities of (a) MoS_2 monolayer and (b) Ni_1/MoS_2. The purple area defines the majority spin (α-spin). (c) Charge density differences of Ni_1/MoS_2. The blue and purple areas represent electron accumulation and depletion, respectively. (d) The 2D charge density difference in vertical *xz* plane, with the color from red to blue representing charges between 0.02 to −0.04 atomic unit (a.u.). (e) The corresponding plane-averaged charge density difference of (d).

Spin-polarized projected DOS (pDOS) reveals that Ni 3d orbitals play a dominant role in bonding with the MoS_2 surface (Fig. 4e), while the Ni 4s/4p states transfer electron density to S and lie much higher in energy. The corresponding partial charge distribution is shown in Fig. 4f, which indeed shows the positively charged Ni atom. The particular pDOS and COHP of Ni d orbitals (z^2, *yz*, *xz*, *xy*, x^2-y^2) are shown in Figs S2 and S3. Both of them indicate that the ionic and covalent bonding interactions between Ni and S atoms of the MoS_2 support lay the foundation for the stability of the SACs.

Based on the band structure, the conducting band minimum (CBM) and valence band maximum (VBM) are situated at the *Γ* points, arising from the Ni atom located at the surface. This electronic feature of Ni single atom is critical for its catalytic performance (*vide infra*). Importantly, there is no state crossing the Fermi level, indicating that the Ni_1/MoS_2 monolayer remains as an indirect gap semiconductor. The symmetric spin states in the DOS imply virtually nonmagnetic behavior of the Ni_1/MoS_2 monolayer as well. From the real space wave functions of the highest occupied molecular orbitals (HOMO) and the lowest unoccupied molecular orbitals (LUMO) at the CBM and VBM (Fig. 4b, d), one can see that the Ni atom has significant orbital distribution at the HOMO of Ni_1/MoS_2, which is viable for catalytic quantum states. Furthermore, the Ni_1/MoS_2 monolayer undergoes change in electrical conductivity with the Ni atom doped, relevant to the electrocatalytic properties.

ELF and work function analysis of Ni_1/MoS_2

In order to further examine the electronic effects of Ni single atom for MoS_2, the electron localization function (ELF) was analyzed in the *xz* plane [80]. It is clear that there is same-spin electron pair density between Mo–S and Ni–S, while the ionicity in the bonds of the MoS_2 monolayer is verified by the ELF value observed with 0.7 around S and 0.4 around Mo atoms (Fig. 5a). In addition, the work function of the surface was calculated by using vaspkit [77], which is an important parameter for evaluating the charge transfer ability of the interface and semiconductor band alignment. The work functions of MoS_2 and Ni_1/MoS_2 can be calculated with the equation [81]:

$$\Phi = E_{vac} - E_F,$$

where Φ is the work function, E_{vac} represents the electrostatic potential of the vacuum, and E_F is the Fermi energy. According to the calculation, the Fermi energy of Ni_1/MoS_2 (Fig. 5c) is higher than that of MoS_2 (Fig. 5b), and the calculated work functions Φ of MoS_2 and Ni_1/MoS_2 are 5.497 and 5.192 eV,

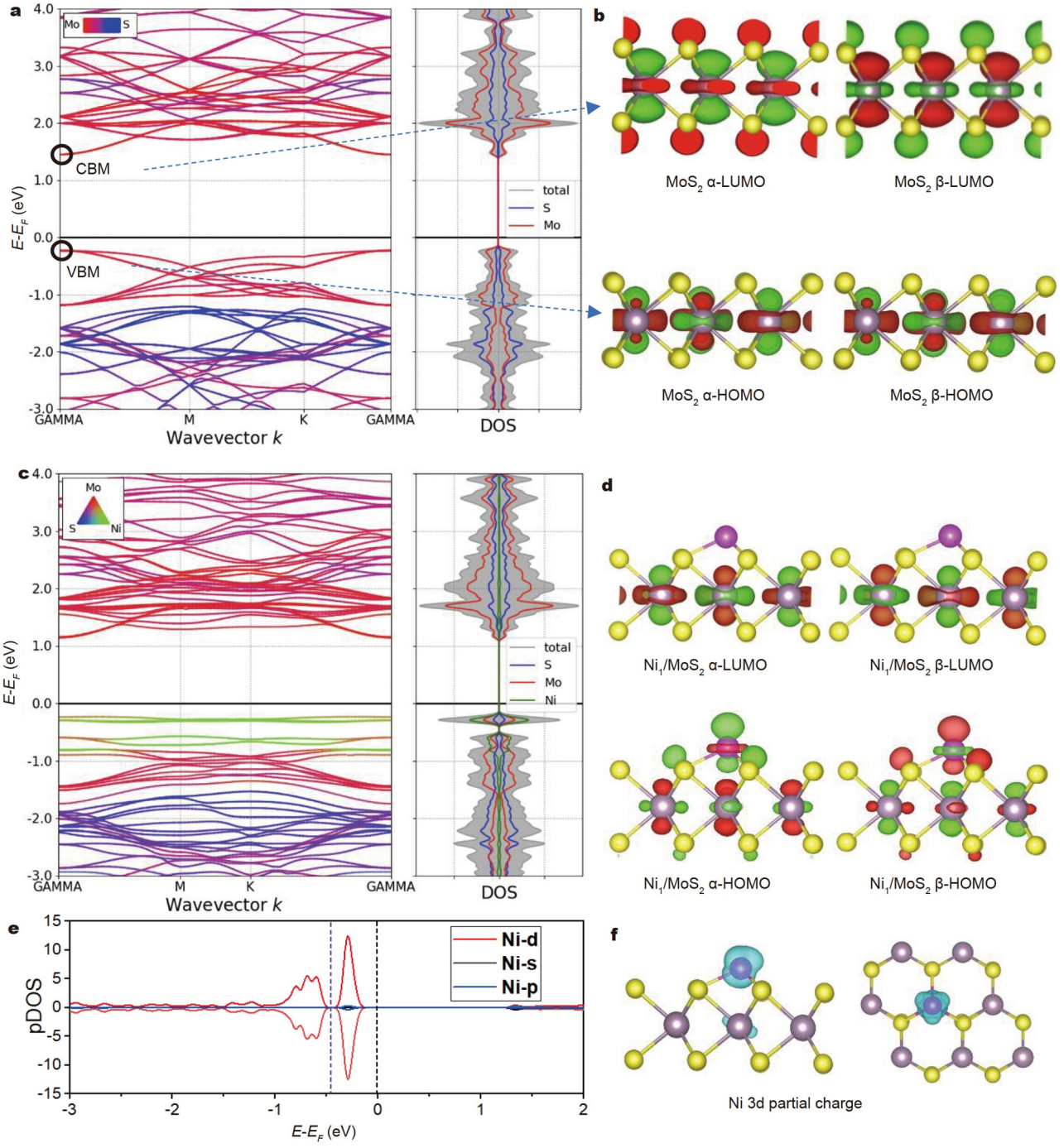

Figure 4 The band structures (with the Fermi energy E_F set to 0) and total DOS of (a) MoS_2 and (c) Ni_1/MoS_2. The α- and β-set real-space wave functions of (b) MoS_2 and (d) Ni_1/MoS_2. (e) The pDOS of Ni (3d, 4s, and 4p) orbitals out of the total DOS. (f) Partial charge distribution of Ni 3d.

respectively. The Ni_1/MoS_2 has lower work function, implying that it is more likely to lose electron compared with MoS_2. Therefore, by supporting Ni atoms on MoS_2, the formed SAC becomes more favorable for the reduction reaction than the support, which can be advantageous for CO_2 reduction.

QTAIM and schematic energy levels of Ni_1/MoS_2

Since SACs have been widely investigated in the past decade, it is interesting to explore the properties of the single atoms and the bonding interaction in Ni_1/MoS_2 by using QTAIM [73]. Based on the topological analysis of the electron density, QTAIM makes it possible to divide a molecule or solid into constituent atoms on the basis of zero-flux surfaces in the one-electron density gradient field $\nabla\rho$. From the saddle-point properties of the electron density function, there are four types of CPs described as following [68]: nuclear CP (NCP), bond CP (BCP), ring CP (RCP), and cage CP (CCP). Fig. 6a exhibits the Hessian of electron density at the various CPs. There are obvious BCP between Ni–S and Mo–S bonds colored in blue, revealing the direct bonding interaction between Ni single atom and the

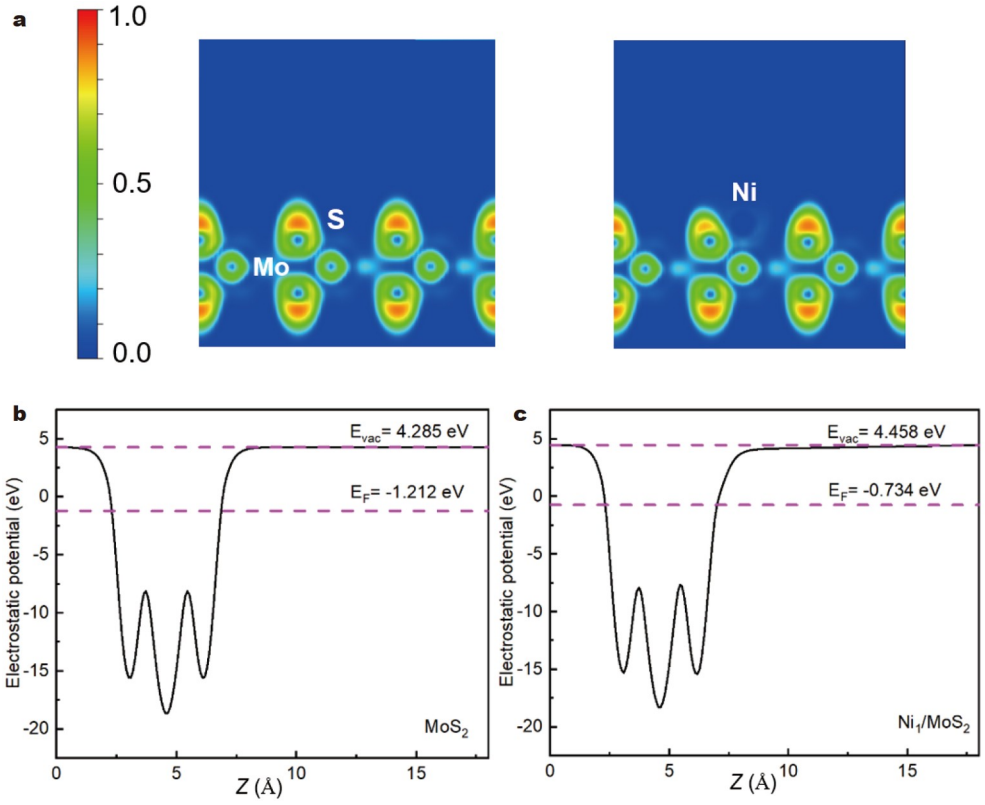

Figure 5 (a) Contour maps of the ELF of MoS_2 and Ni_1/MoS_2. The probability of same-spin pair density varies from 0 (blue) to 1.0 (red). Electrostatic potentials and work functions of (b) MoS_2 and (c) Ni_1/MoS_2.

support. In addition, RCP and CCP can also be observed as shown by the gray color. The quantified electron density at the cut-plane containing Ni–S–Mo–S is shown in Fig. 6b. To investigate the bonding interaction between Ni and the nearest neighboring atoms, the BCPs (red dots) and RCPs (green dots) are shown in Fig. 6c. It is interesting to note that in addition to the BCPs of Ni–S and Mo–S, there exists unexpected BCP of Ni–Mo, which implies that the bonding interaction between Ni and Mo atoms also plays a critical role in the electronic structure and catalytic performance of Ni_1/MoS_2. While CMSI mainly occurs between metal single-atom (M_1) and the nonmetal element of the support, this kind of direct metal–metal (here Ni–Mo) bonding has not been fully recognized. This interaction will further enhance the binding and stability of Ni single atom on the MoS_2 support, and regulates the catalytic properties of Ni_1/MoS_2.

The electron density values at the BCP $\rho(r_{bcp})$, which indicates the strength of the chemical bond, and Laplacian values of the electron density $\nabla^2\rho(r_{bcp})$ related to the ionic/covalent nature of the bonding as well as the key QTAIM parameters are listed in Table 1. The eigenvalues of the corresponding Hessian matrix are marked as λ_1, λ_2, and λ_3. The ellipticity of a bond is calculated as $\varepsilon = |\lambda_1|/|\lambda_2| - 1$, which characterizes the electron delocalization of the bond under consideration. The $\rho(r_{bcp})$ values decrease in the order of Ni–S > Mo–S > Ni–Mo, indicating that the Ni–Mo bonding is the weakest compared with the bonding of Ni–S and Mo–S. The $\nabla^2\rho(r_{bcp})$ values for Ni–S, Ni–Mo and Mo–S are all positive, with $|\lambda_1|/|\lambda_3| < 1$, indicating that the bonding interactions are primarily ionic bonds, dominated by the contraction of charge away from the BCP toward each of the nuclei [73]. For Ni–S and Ni–Mo, the ellipticity of the bonds are relatively small, ε = 0.057 and 0, respectively, which implies that they behave as σ single bonds because of the cylindrical shape of the bond cross section. The ε reaching 0.294 at Mo–S BCP is interpreted as a measure of the π character because from the single to double bond, the cross section tends to be more elliptic, reaching maximal ellipticity for a typical double bond [82].

The schematic energy levels are presented in Fig. 6d. From the DOS (Fig. 4c) and COHP results, S-2p states are located at the low-energy region of Ni_1/MoS_2, while the bands of Ni-3d and Mo-4d orbitals are broadened by the orbital overlap between Ni or Mo and S atoms. While Ni-3d band is fully occupied, the Mo-4d band is not completely filled, so there exist both occupied and unoccupied states around the Fermi level, consistent with the Mo(IV) oxidation state. Meanwhile, the Ni-4s,4p and Mo-5s,5p orbitals mainly contribute to the unoccupied states in Ni_1/MoS_2 due to the electron transfer and orbital mixing with S orbitals.

Electrocatalytic CO_2RR with Ni_1/MoS_2

The electronic structure features of Ni_1/MoS_2 indicate that this non-noble metal SAC is both stable and reactive for reduction reactions. Therefore, the performance of Ni_1/MoS_2 was evaluated for electrocatalytic CO_2RR. The reaction mechanism of CO_2RR on the Ni_1/MoS_2 catalyst was investigated *via* the CHE model and DFT calculations with PBE functional. The reaction mechanism is summarized in Fig. 7, where the formation of methanol turns out to be the preferred pathway. Here the Ni atoms are found to have highly active catalytic sites for CO_2RR. For electrocatalytic CO_2RR, HER is a potential competing

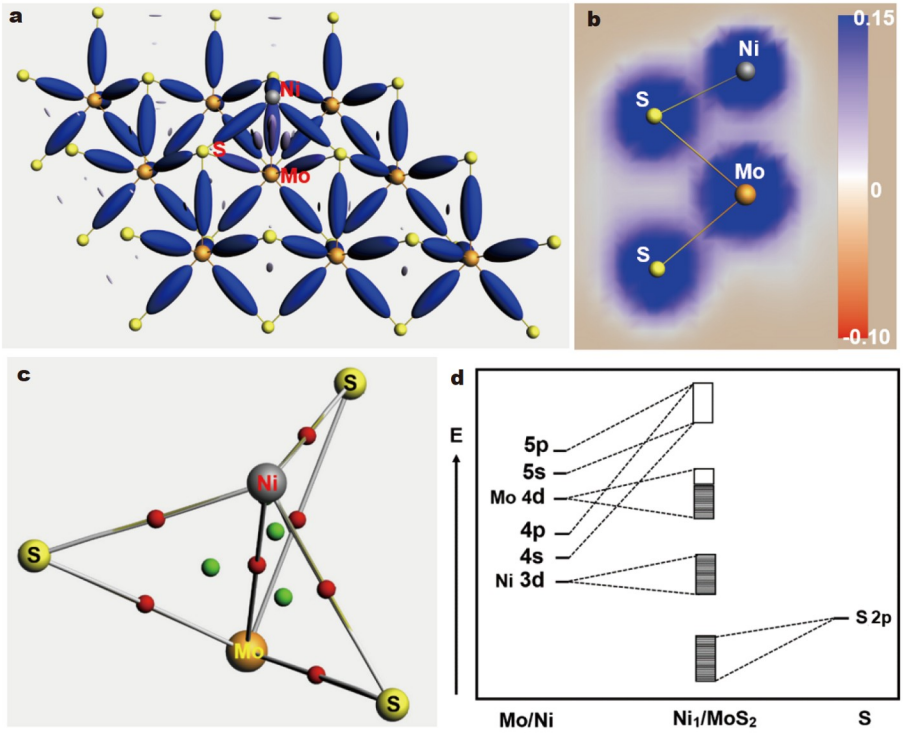

Figure 6 The results of topological analysis of the electron density. (a) Ni_1/MoS_2 Hessian of electron density at various CPs. (b) The electron density at the cut-plane containing Ni–S–Mo–S. (c) The BCPs (red dots) of Ni–S, Ni–Mo, and Mo–S, and the three RCPs (green dots) from QTAIM analysis. (d) Schematic energy levels showing the orbital interaction between Ni or Mo and S atoms.

Table 1 The electron density values at BCP ($\rho(r_{bcp})$), Laplacian values of the density ($\nabla^2\rho(r_{bcp})$), eigenvalues of the Hessian matrix, ratio values between the perpendicular and the parallel curvatures ($|\lambda_1|/|\lambda_3|$) of Ni_1/MoS_2 calculated by using PBE/TZ2P. All quantities are given in a.u.

bcp	$\rho(r_{bcp})$	$\nabla^2\rho(r_{bcp})$	ε	λ_1	λ_2	λ_3	$\lvert\lambda_1\rvert/\lvert\lambda_3\rvert$
Ni–S	0.105	0.212	0.057	−0.111	−0.105	0.428	0.259
Ni–Mo	0.056	0.103	0.000	−0.029	−0.029	0.161	0.180
Mo–S	0.071	0.123	0.294	−0.066	−0.051	0.240	0.275

process. As shown in Fig. S4, the ΔG for the desorption of H* on Ni_1/MoS_2 for HER is higher than that for $*CO_2$. Therefore, as shown in Fig. 7a, with CO_2 adsorption on the Ni atom of Ni_1/MoS_2, it gets activated by η^2-π-bonding with the Ni atom. The chemisorbed $*CO_2$ can further react with $H^+ + e^-$ to form *COOH, which will form adsorbed *CO and H_2O when the OH is attacked by another $H^+ + e^-$. Interestingly, because *CO is strongly bound by the Ni atom *via* 5σ-donation and 2π-back-donation, its desorption from the catalytic sites to generate CO gas is partially suppressed. Instead, hydrogenation of Ni-bonded *CO by $H^+ + e^-$ leads to the formation of *CHO, which is beneficial to further catalytic reaction towards methanol. The different reaction pathways involving intermediates *C(OH), CO(g), $*CH_2O$, *CHOH, $*CH_3O$, $*CH_2OH$, $*CH_4O$ and $*CH_3OH$ were examined (Fig. 7b). For the optimal reaction pathway, the following steps occur:

$$CO_2 + * \rightarrow *CO_2, \quad (1)$$

$$*CO_2 + H^* \rightarrow *COOH, \quad (2)$$

$$*COOH + H^* \rightarrow *CO + H_2O, \quad (3)$$

$$*CO + H^* \rightarrow *CHO, \quad (4)$$

$$*CHO + H^* \rightarrow *CH_2O, \quad (5)$$

$$*CH_2O + H^* \rightarrow *CH_3O, \quad (6)$$

$$*CH_3O + H^* \rightarrow *CH_3OH, \quad (7)$$

$$*CH_3OH \rightarrow CH_3OH + *. \quad (8)$$

Compared with the electronic structure of Ni_1/MoS_2 as discussed before, the Ni_1 doping on MoS_2 changes the charge and spin densities, which favors strong adsorption of CO, resulting in superior electrocatalytic CO_2RR performance toward methanol [83,84].

CONCLUSIONS

Heterogeneous SACs have recently aroused significant interest and become the frontier in catalysis science. This novel kind of catalysts provides an opportunity for tuning the catalytic properties using the surface atoms of the support. Therefore, developing non-noble metal catalysts *via* the idea of SACs looks promising. In this article, the first principles quantum theory has been used to computationally screen M_1/MoS_2 (M_1 = Sc, Ti, V, Cr, Mn, Fe, Co, Ni, Cu, Zn) with the first series of transition metals. The electronic structure of Ni_1/MoS_2 has been studied in

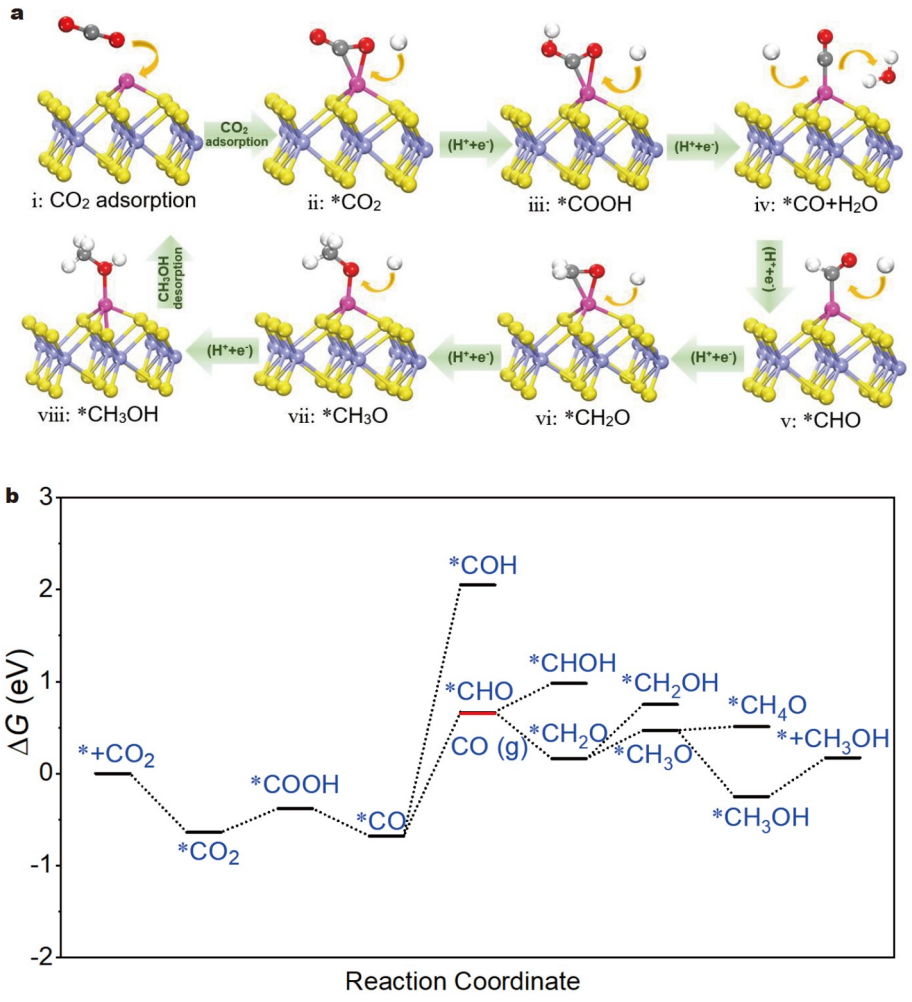

Figure 7 The reaction mechanism for CO_2RR into CH_3OH on Ni_1/MoS_2. (a) The structures of the reaction intermediates; (b) the energy profile for different pathways calculated using the CHE model and DFT method with PBE functional.

details using solid state analysis approaches, including ELF, DOS, and band structure. The bonding interactions have been further examined by using COHP and QTAIM. The spin densities and charge density difference have been changed with Ni_1 doped on MoS_2, which influences the electrocatalytic performance for CO_2RR. The optimal reaction pathway of CO_2RR to methanol has also been investigated. The Ni single atoms have exhibited highly active catalytic sites for this reaction. Further exploration of this kind of non-noble metal SACs for other reduction reactions would be interesting.

Received 4 July 2022; accepted 4 August 2022; published online 4 November 2022

1 Voiry D, Goswami A, Kappera R, *et al.* Covalent functionalization of monolayered transition metal dichalcogenides by phase engineering. Nat Chem, 2015, 7: 45–49
2 Yang Y, Wang G, Huang W, *et al.* Reversible optical control of the metal-insulator transition across the epitaxial heterointerface of a VO_2/Nb:TiO_2 junction. Sci China Mater, 2021, 64: 1687–1702
3 Aljarb A, Fu JH, Hsu CC, *et al.* Ledge-directed epitaxy of continuously self-aligned single-crystalline nanoribbons of transition metal dichalcogenides. Nat Mater, 2020, 19: 1300–1306
4 Zhang M, Lihter M, Chen TH, *et al.* Super-resolved optical mapping of reactive sulfur-vacancies in two-dimensional transition metal dichalcogenides. ACS Nano, 2021, 15: 7168–7178
5 Mak KF, Shan J. Photonics and optoelectronics of 2D semiconductor transition metal dichalcogenides. Nat Photon, 2016, 10: 216–226
6 Wang J, Zhang Z, Ding J, *et al.* Recent progresses of micro-nano-structured transition metal compound-based electrocatalysts for energy conversion technologies. Sci China Mater, 2021, 64: 1–26
7 Shuai H, Li J, Jiang F, *et al.* Electrochemically intercalated intermediate induced exfoliation of few-layer MoS_2 from molybdenite for long-life sodium storage. Sci China Mater, 2021, 64: 115–127
8 Chen B, Wang T, Zhao S, *et al.* Efficient reversible conversion between MoS_2 and Mo/Na_2S enabled by graphene-supported single atom catalysts. Adv Mater, 2021, 33: 2007090
9 Niu S, Jiang WJ, Tang T, *et al.* Autogenous growth of hierarchical NiFe$(OH)_x$/FeS nanosheet-on-microsheet arrays for synergistically enhanced high-output water oxidation. Adv Funct Mater, 2019, 29: 1902180
10 Peng J, Liu Y, Pan Y, *et al.* Fast lithium ion conductivity in layered (Li-Ag)CrS_2. J Am Chem Soc, 2020, 142: 18645–18651
11 Liang J, Wang Y, Liu Q, *et al.* Electrocatalytic hydrogen peroxide production in acidic media enabled by NiS_2 nanosheets. J Mater Chem A, 2021, 9: 6117–6122
12 Lin Y, Adilbekova B, Firdaus Y, *et al.* 17% Efficient organic solar cells based on liquid exfoliated WS_2 as a replacement for PEDOT:PSS. Adv Mater, 2019, 31: 1902965
13 He H, Chen C, Chen Z, *et al.* Ni_3S_2@S-carbon nanotubes synthesized using NiS_2 as sulfur source and precursor for high performance so-

dium-ion half/full cells. Sci China Mater, 2020, 63: 216–228
14 Chu K, Liu YP, Li YB, *et al.* Two-dimensional (2D)/2D interface engineering of a MoS_2/C_3N_4 heterostructure for promoted electrocatalytic nitrogen fixation. ACS Appl Mater Interfaces, 2020, 12: 7081–7090
15 Tang B, Zhao Y, Zhou C, *et al.* Threshold voltage modulation in monolayer MoS_2 field-effect transistors *via* selective gallium ion beam irradiation. Sci China Mater, 2022, 65: 741–747
16 Guo Y, Tang J, Henzie J, *et al.* Mesoporous iron-doped $MoS_2/CoMo_2S_4$ heterostructures through organic-metal cooperative interactions on spherical micelles for electrochemical water splitting. ACS Nano, 2020, 14: 4141–4152
17 Schauble K, Zakhidov D, Yalon E, *et al.* Uncovering the effects of metal contacts on monolayer MoS_2. ACS Nano, 2020, 14: 14798–14808
18 Chen X, Zang J, Yang X, *et al.* Ultrasensitive monolayer-MoS_2 heterojunction photodetectors realized *via* an asymmetric Fabry-Perot cavity. Sci China Mater, 2022, 65: 1861–1868
19 Hong X, Chan K, Tsai C, *et al.* How doped MoS_2 breaks transition-metal scaling relations for CO_2 electrochemical reduction. ACS Catal, 2016, 6: 4428–4437
20 Mao X, Wang L, Xu Y, *et al.* Modulating the MoS_2 edge structures by doping transition metals for electrocatalytic CO_2 reduction. J Phys Chem C, 2020, 124: 10523–10529
21 Li H, Tsai C, Koh AL, *et al.* Activating and optimizing MoS_2 basal planes for hydrogen evolution through the formation of strained sulphur vacancies. Nat Mater, 2016, 15: 48–53
22 Yu XY, Hu H, Wang Y, *et al.* Ultrathin MoS_2 nanosheets supported on N-doped carbon nanoboxes with enhanced lithium storage and electrocatalytic properties. Angew Chem, 2015, 127: 7503–7506
23 Seh ZW, Kibsgaard J, Dickens CF, *et al.* Combining theory and experiment in electrocatalysis: Insights into materials design. Science, 2017, 355: 4998
24 Escalera-López D, Niu Y, Yin J, *et al.* Enhancement of the hydrogen evolution reaction from Ni-MoS_2 hybrid nanoclusters. ACS Catal, 2016, 6: 6008–6017
25 Qiao BT, Wang AQ, Yang X, *et al.* Single-atom catalysis of CO oxidation using Pt_1/FeO_x. Nat Chem, 2011, 3: 634–641
26 Xu Q, Guo CX, Tian S, *et al.* Coordination structure dominated performance of single-atomic Pt catalyst for anti-Markovnikov hydroboration of alkenes. Sci China Mater, 2020, 63: 972–981
27 Li J, Li Y, Zhang T. Recent progresses in the research of single-atom catalysts. Sci China Mater, 2020, 63: 889–891
28 Zhuo HY, Zhang X, Liang JX, *et al.* Theoretical understandings of graphene-based metal single-atom catalysts: Stability and catalytic performance. Chem Rev, 2020, 120: 12315–12341
29 Li Z, Ji S, Liu Y, *et al.* Well-defined materials for heterogeneous catalysis: From nanoparticles to isolated single-atom sites. Chem Rev, 2020, 120: 623–682
30 Ren S, Yu Q, Yu X, *et al.* Graphene-supported metal single-atom catalysts: A concise review. Sci China Mater, 2020, 63: 903–920
31 Chen S, Kang Z, Hu X, *et al.* Delocalized spin states in 2D atomic layers realizing enhanced electrocatalytic oxygen evolution. Adv Mater, 2017, 29: 1701687
32 Li X, Cao CS, Hung SF, *et al.* Identification of the electronic and structural dynamics of catalytic centers in single-Fe-atom material. Chem, 2020, 6: 3440–3454
33 Rong P, Jiang YF, Wang Q, *et al.* Photocatalytic degradation of methylene blue (MB) with Cu_1-ZnO single atom catalysts on graphene-coated flexible substrates. J Mater Chem A, 2022, 10: 6231–6241
34 Gong YN, Zhong W, Li Y, *et al.* Regulating photocatalysis by spin-state manipulation of cobalt in covalent organic frameworks. J Am Chem Soc, 2020, 142: 16723–16731
35 Chen Y, Huang Z, Gu X, *et al.* Top-down synthesis strategies: Maximum noble-metal atom efficiency in catalytic materials. Chin J Catal, 2017, 38: 1588–1596
36 Zhou S, Jang H, Qin Q, *et al.* Three-dimensional hierarchical Co(OH)F nanosheet arrays decorated by single-atom Ru for boosting oxygen evolution reaction. Sci China Mater, 2021, 64: 1408–1417
37 Yang ZK, Wang XL, Zhu MZ, *et al.* Structural revolution of atomically dispersed Mn sites dictates oxygen reduction performance. Nano Res, 2021, 14: 4512–4519
38 Yang J, Wang ZY, Huang CX, *et al.* Compressive strain modulation of single iron sites on helical carbon support boosts electrocatalytic oxygen reduction. Angew Chem Int Ed, 2021, 60: 22722–22728
39 Zhu MZ, Zhao C, Liu XK, *et al.* Single atomic cerium sites with a high coordination number for efficient oxygen reduction in proton-exchange membrane fuel cells. ACS Catal, 2021, 11: 3923–3929
40 Xue ZG, Yan MY, Wang XL, *et al.* Tailoring unsymmetrical-coordinated atomic site inoxide-supported Pt catalysts for enhanced surface activity and stability. Small, 2021, 17: 2101008
41 Li Y, Gu Q, Johannessen B, *et al.* Synergistic Pt doping and phase conversion engineering in two-dimensional MoS_2 for efficient hydrogen evolution. Nano Energy, 2021, 84: 105898
42 Jiao D, Liu Y, Cai Q, *et al.* Coordination tunes the activity and selectivity of the nitrogen reduction reaction on single-atom iron catalysts: A computational study. J Mater Chem A, 2021, 9: 1240–1251
43 Huang CX, Li GL, Yang LM, *et al.* Ammonia synthesis using single-atom catalysts based on two-dimensional organometallic metal phthalocyanine monolayers under ambient conditions. ACS Appl Mater Interfaces, 2021, 13: 608–621
44 Xu L, Yang LM, Ganz E. Electrocatalytic reduction of N_2 using metal-doped borophene. ACS Appl Mater Interfaces, 2021, 13: 14091–14101
45 Zhao MR, Song BY, Yang LM. Two-dimensional single-atom catalyst $TM_3(HAB)_2$ monolayers for electrocatalytic dinitrogen reduction using hierarchical high-throughput screening. ACS Appl Mater Interfaces, 2021, 13: 26109–26122
46 Lv SY, Huang CX, Li GL, *et al.* Electrocatalytic mechanism of N_2 reduction reaction by single-atom catalyst rectangular TM-TCNQ monolayers. ACS Appl Mater Interfaces, 2021, 13: 29641–29653
47 Lv SY, Li GL, Yang LM. Transition metals embedded two-dimensional square tetrafluorotetracyanoquinodimethane monolayers as a class of novel electrocatalysts for nitrogen reduction reaction. ACS Appl Mater Interfaces, 2022, 14: 25317–25325
48 Wang XL, Yang LM. Unveiling the underlying mechanism of nitrogen fixation by a new class of electrocatalysts two-dimensional TM@g-C_4N_3 monosheets. Appl Surf Sci, 2022, 576: 151839
49 Lv SY, Huang CX, Li GL, *et al.* Unveiling the underlying mechanism of transition metal atoms anchored square tetracyanoquinodimethane monolayers as electrocatalysts for N_2 fixation. Energy Environ Mater, 2022, 5: 533–542
50 Wang XL, Yang LM. Efficient modulation of the catalytic performance of electrocatalytic nitrogen reduction with transition metals anchored on N/O-codoped graphene by coordination engineering. J Mater Chem A, 2022, 10: 1481–1496
51 Huang CX, Lv SY, Li C, *et al.* Single-atom catalysts based on two-dimensional metalloporphyrin monolayers for ammonia synthesis under ambient conditions. Nano Res, 2022, 15: 4039–4047
52 Lv SY, Li GL, Yang LM. Prognostication of two-dimensional transition-metal atoms embedded rectangular tetrafluorotetracyanoquinodimethane single-atom catalysts for high-efficiency electrochemical nitrogen reduction. J Colloid Interface Sci, 2022, 621: 24–32
53 Liu Y, Song BY, Huang CX, *et al.* Dual transition metal atoms embedded in N-doped graphene for electrochemical nitrogen fixation under ambient conditions. J Mater Chem A, 2022, 10: 13527–13543
54 Li M, Wang H, Luo W, *et al.* Heterogeneous single-atom catalysts for electrochemical CO_2 reduction reaction. Adv Mater, 2020, 32: 2001848
55 Yang J, Wang XL, Qu YT, *et al.* Bi-based metal-organic framework derived leafy bismuth nanosheets for carbon dioxide electroreduction. Adv Energy Mater, 2020, 10: 2001709
56 Liu JH, Yang LM, Ganz E. Efficient and selective electroreduction of CO_2 by single-atom catalyst two-dimensional TM-Pc monolayers. ACS Sustain Chem Eng, 2018, 6: 15494–15502
57 Liu JH, Yang LM, Ganz E. Electrochemical reduction of CO_2 by single atom catalyst TM-TCNQ monolayers. J Mater Chem A, 2019, 7: 3805–3814
58 Liu JH, Yang LM, Ganz E. Electrocatalytic reduction of CO_2 by two-dimensional transition metal porphyrin sheets. J Mater Chem A, 2019, 7: 11944–11952

59 Liu JH, Yang LM, Ganz E. Two-dimensional organometallic TM_3-$C_{12}S_{12}$ monolayers for electrocatalytic reduction of CO_2. Energy Environ Mater, 2019, 2: 193–200
60 Liu JH, Yang LM, Ganz E. Efficient electrocatalytic reduction of carbon dioxide by metal-doped β_{12}-borophene monolayers. RSC Adv, 2019, 9: 27710–27719
61 Lu Y, Wang J, Yu L, *et al.* Identification of the active complex for Co oxidation over single-atom Ir-on-$MgAl_2O_4$ catalysts. Nat Catal, 2019, 2: 149–156
62 Zheng T, Jiang K, Wang H. Recent advances in electrochemical CO_2-to-CO conversion on heterogeneous catalysts. Adv Mater, 2018, 30: 1802066
63 Zhao Q, Zhang C, Hu R, *et al.* Selective etching quaternary MAX phase toward single atom copper immobilized MXene ($Ti_3C_2Cl_x$) for efficient CO_2 electroreduction to methanol. ACS Nano, 2021, 15: 4927–4936
64 Zhang S, Kang P, Ubnoske S, *et al.* Polyethylenimine-enhanced electrocatalytic reduction of CO_2 to formate at nitrogen-doped carbon nanomaterials. J Am Chem Soc, 2014, 136: 7845–7848
65 Kresse G, Furthmüller J. Efficient iterative schemes for *ab initio* total-energy calculations using a plane-wave basis set. Phys Rev B, 1996, 54: 11169–11186
66 Kresse G, Furthmüller J. Efficiency of *ab-initio* total energy calculations for metals and semiconductors using a plane-wave basis set. Comput Mater Sci, 1996, 6: 15–50
67 Perdew JP, Burke K, Ernzerhof M. Generalized gradient approximation made simple. Phys Rev Lett, 1996, 77: 3865–3868
68 Bader RFW. A quantum theory of molecular structure and its applications. Chem Rev, 1991, 91: 893–928
69 Maintz S, Deringer VL, Tchougréeff AL, *et al.* Lobster: A tool to extract chemical bonding from plane-wave based DFT. J Comput Chem, 2016, 37: 1030–1035
70 Nørskov JK, Rossmeisl J, Logadottir A, *et al.* Origin of the overpotential for oxygen reduction at a fuel-cell cathode. J Phys Chem B, 2004, 108: 17886–17892
71 Peterson AA, Nørskov JK. Activity descriptors for CO_2 electroreduction to methane on transition-metal catalysts. J Phys Chem Lett, 2012, 3: 251–258
72 Baerends EJ, Ziegler T, Autschbach J, *et al.* ADF2017, SCM, Theoretical Chemistry. Amsterdam: Vrije Universiteit, 2014
73 Bader RFW. Atoms in Molecules: A Quantum Theory. Oxford: Clarendon Press, 1994
74 Qiao B, Liang JX, Wang AQ, *et al.* Ultrastable single-atom gold catalysts with strong covalent metal-support interaction (CMSI). Nano Res, 2015, 8: 2913–2924
75 Dang Q, Tang S, Liu T, *et al.* Regulating electronic spin moments of single-atom catalyst sites *via* single-atom promoter tuning on S-vacancy MoS_2 for efficient nitrogen fixation. J Phys Chem Lett, 2021, 12: 8355–8362
76 Wang L, Guan E, Zhang J, *et al.* Single-site catalyst promoters accelerate metal-catalyzed nitroarene hydrogenation. Nat Commun, 2018, 9: 1362
77 Wang V, Xu N, Liu JC, *et al.* VASPKIT: A user-friendly interface facilitating high-throughput computing and analysis using VASP code. Comput Phys Commun, 2021, 267: 108033
78 Lin S, Ye X, Johnson RS, *et al.* First-principles investigations of metal (Cu, Ag, Au, Pt, Rh, Pd, Fe, Co, and Ir) doped hexagonal boron nitride nanosheets: Stability and catalysis of Co oxidation. J Phys Chem C, 2013, 117: 17319–17326
79 Liu S, Huang S. Atomically dispersed Co atoms on MoS_2 monolayer: A promising high-activity catalyst for CO oxidation. Appl Surf Sci, 2017, 425: 478–483
80 Becke AD, Edgecombe KE. A simple measure of electron localization in atomic and molecular systems. J Chem Phys, 1990, 92: 5397–5403
81 Liu J, Cheng B, Yu J. A new understanding of the photocatalytic mechanism of the direct Z-scheme g-C_3N_4/TiO_2 heterostructure. Phys Chem Chem Phys, 2016, 18: 31175–31183
82 Popelier PLA. Atoms in molecules: An introduction. Pearson Education, Harlow, UK, 2000. 144–197
83 Xie JF, Zhao XT, Wu MX, *et al.* Metal-free fluorine-doped carbon electrocatalyst for CO_2 reduction outcompeting hydrogen evolution. Angew Chem Int Ed, 2018, 57: 9640–9644
84 Lv K, Teng C, Shi M, *et al.* Hydrophobic and electronic properties of the E-MoS_2 nanosheets induced by FAS for the CO_2 electroreduction to syngas with a wide range of CO/H_2 ratios. Adv Funct Mater, 2018, 28: 1802339

Acknowledgements I thank Assoc. Prof. Hai Xiao and Dr. Zhaoming Xia for their helpful discussion. This work was financially supported by the National Natural Science Foundation of China (92061109), the Natural Science Basic Research Program of Shaanxi (2021JCW-20 and S2020-JC-WT-0001), the Open Project Program of Fujian Key Laboratory of Functional Marine Sensing Materials (MJUKF-FMSM202002), and Guangdong Provincial Key Laboratory of Catalysis (2020B121201002). Computational resources are provided by Beijing Clouds Supercomputing Center.

Author contributions Yu Q designed the project, performed the calculations and wrote the paper.

Conflict of interest The author declares no conflict of interest.

Supplementary information Supporting data are available in the online version of the paper.

Qi Yu obtained her BSc (2008), MSc (2010) and PhD (2013) degrees from Jilin University, China. She is currently a professor at the Institute of Graphene at Shaanxi Key Laboratory of Catalysis, Shaanxi University of Technology. Her research interests include theoretical investigations on graphene materials and electrocatalysis with single-atom catalysts.

非贵金属单原子催化剂Ni_1/MoS_2的电子结构及CO_2还原电催化性能

于琦*

摘要 单原子催化剂(SACs)因其在化学反应中具有高选择性及催化活性, 近年来在多相催化领域已引起广泛关注. 本文采用第一性原理理论计算, 对MoS_2负载的非贵金属SACs进行计算化学筛选, 考察了3d金属单原子(M = Sc, Ti, V, Cr, Mn, Fe, Co, Ni, Cu, Zn)负载的SACs的稳定性. 我们发现, Ni_1/MoS_2催化剂具有最佳的结合能, 在此3d系列催化剂结构中最稳定. 为分析SACs的稳定性与成键作用, 本文系统地研究了Ni_1/MoS_2的电子结构, 包括使用自旋密度、电荷密度差分(CDD)、电子局域化函数(ELF)、能带结构、态密度(DOS)以及局部晶体轨道哈密顿量(COHP). 此外, 还应用分子中原子的固态量子理论(QTAIM)进一步表征了Ni–S、Ni–Mo及Mo–S键的共价性与离子性. 此外, 为研究Ni_1/MoS_2的电催化应用, 对CO_2还原反应(CO_2RR)制甲醇的反应机理与路径进行了分析. 计算表明, Ni_1/MoS_2对于CO_2RR具有较高的催化活性. 本文为MoS_2基功能材料高效SACs的设计提供了理论依据.

